Supporting Information

Large Conductance Variations in a Mechanosensitive Single–Molecule Junction

Davide Stefani, Kevin J. Weiland, Maxim Skripnik, Chunwei Hsu, Mickael L. Perrin, Marcel Mayor, Fabian Pauly and Herre S. J. van der Zant

Supporting Section I. Synthesis and Characterisation

1. General remarks

All compounds, if commercially available, were used as received. 4-Acetylthioiodobenzene and 4,12-bisethynyl[2.2]paracyclophane were synthesised according to literature known procedures.[1,2] ^{1}H- and ^{13}C-NMR spectra were recorded on an *Oxford 400 MHz NMR* with an *Avance III 400 spectrometer*. The chemical shifts are reported in parts per million (ppm) relative to the residual solvent peak and the *J* values are given in Hz (± 0.1 Hz). Deuterated CD_2Cl_2 was purchased from *Sigma Aldrich*. The spectra were recorded at 298 K. High resolution ESI-TOF was performed on a *Bruker maxis*^{TM} *4G*. The melting point was measured on a *Büchi M-565* melting point apparatus and is uncorrected. The MS spectrum was measured in *m/z* (%). Silica gel for column chromatography (40-63 μm, 230-400 mesh) was purchased from *Silicycle Inc* and TLC was performed on TLC silica gel 60 F_{254} aluminium sheets from *Merck KGaA*.

2. Synthetic procedure and analytical data

To a stirred solution of CuI (2.79 mg, 14.6 μmol, 0.05 eq), $Pd(PPh_3)_4$ (33.9 mg, 29.3 μmol, 0.1 eq), and 4-acetylthioiodobenzene (204 mg, 732 μmol, 2.5 eq) in 10 mL THF (7.5 mL) and diisopropylamine (2.5 mL) under Ar was added 4,12-bisethynyl[2.2]paracyclophane (75 mg,

293 µmol, 1.0 eq). The reaction mixture was heated to 55 °C overnight. Subsequently, it was cooled to room temperature, filtered through a plug of celite, and the solvent was removed under reduced pressure. The crude product was purified by column chromatography in toluene/CH_2Cl_2 (1:1). 4,12-bis(((4'-acetylthio)phenyl)ethynyl)[2.2]paracyclophane was isolated as a white solid (88 mg, 158 µmol, 54%). mp: 192-193 °C; ^{1}H NMR (400 MHz, CD_2Cl_2): δ 7.67 – 7.62 (m, 4H), 7.48 – 7.44 (m, 4H), 7.04 (dd, *J* = 7.9, 1.9 Hz, 2H), 6.63 (d, *J* = 1.9 Hz, 2H), 6.54 (d, *J* = 7.9 Hz, 2H), 3.67 (ddd, *J* = 13.1, 10.4, 2.9 Hz, 2H), 3.23 (ddd, *J* = 12.8, 10.4, 4.6 Hz, 2H), 3.12 – 2.91 (m, 4H), 2.44 (s, 6H); ^{13}C NMR (101 MHz, CD_2Cl_2) δ 193.98, 143.03, 140.32, 137.82, 135.04, 133.81, 132.47, 131.25, 128.74, 125.52, 124.83, 92.55, 91.99, 34.58, 34.41, 30.69; HRMS (ESI, +): *m/z* calcd. for $C_{36}H_{28}NaO_2S_2$ $[M+Na]^+$ 579.1429; found: 579.1423.

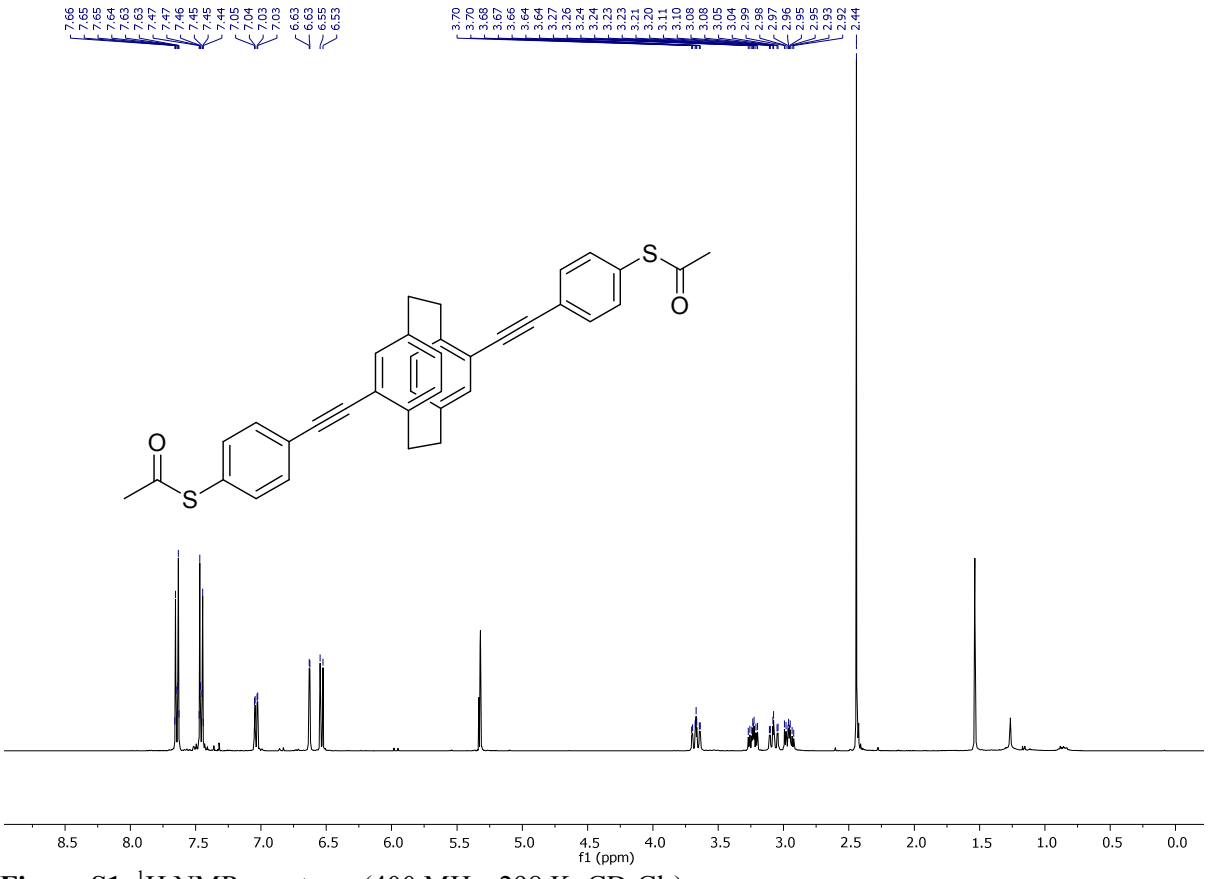

Figure S1. ^{1}H NMR spectrum (400 MHz, 298 K; CD_2Cl_2).

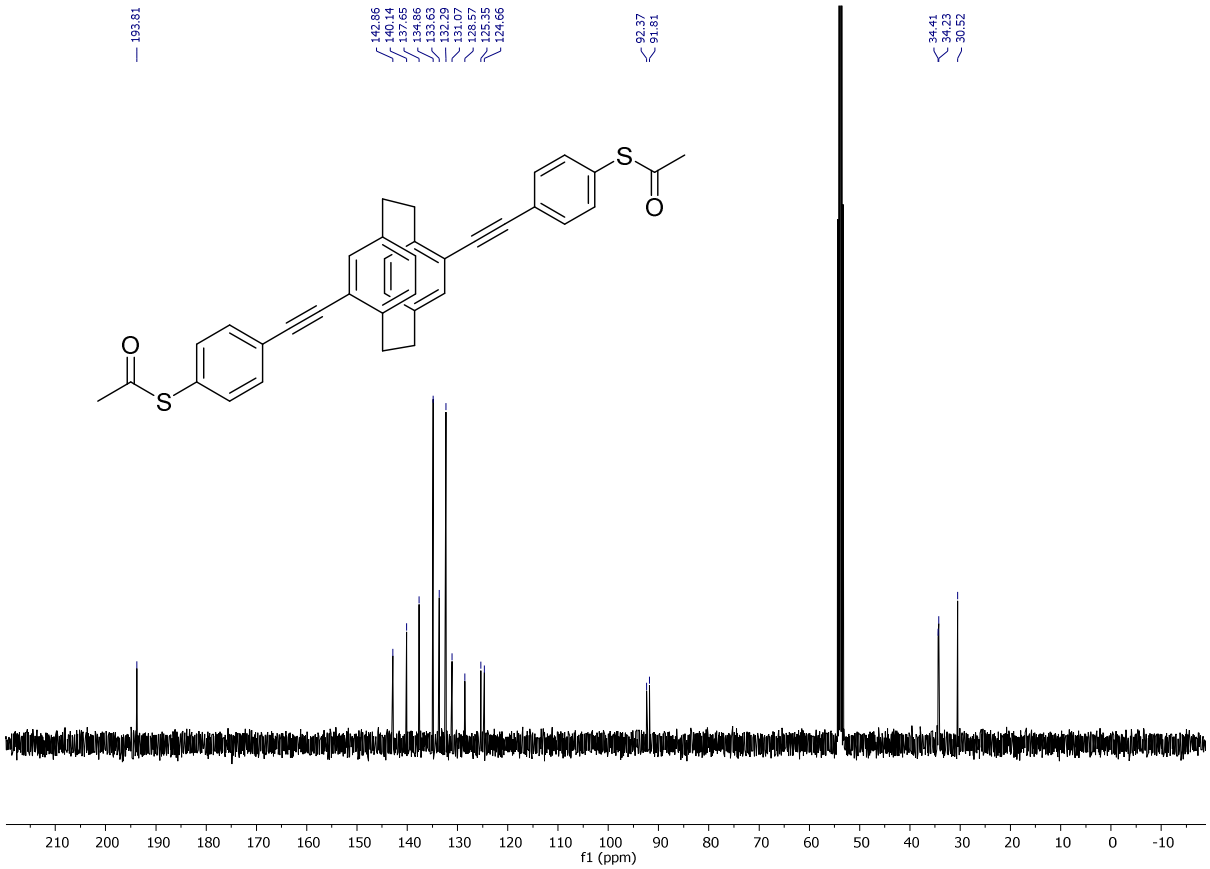

Figure S2. ^{13}C NMR spectrum (126 MHz, 298 K; CD_2Cl_2).

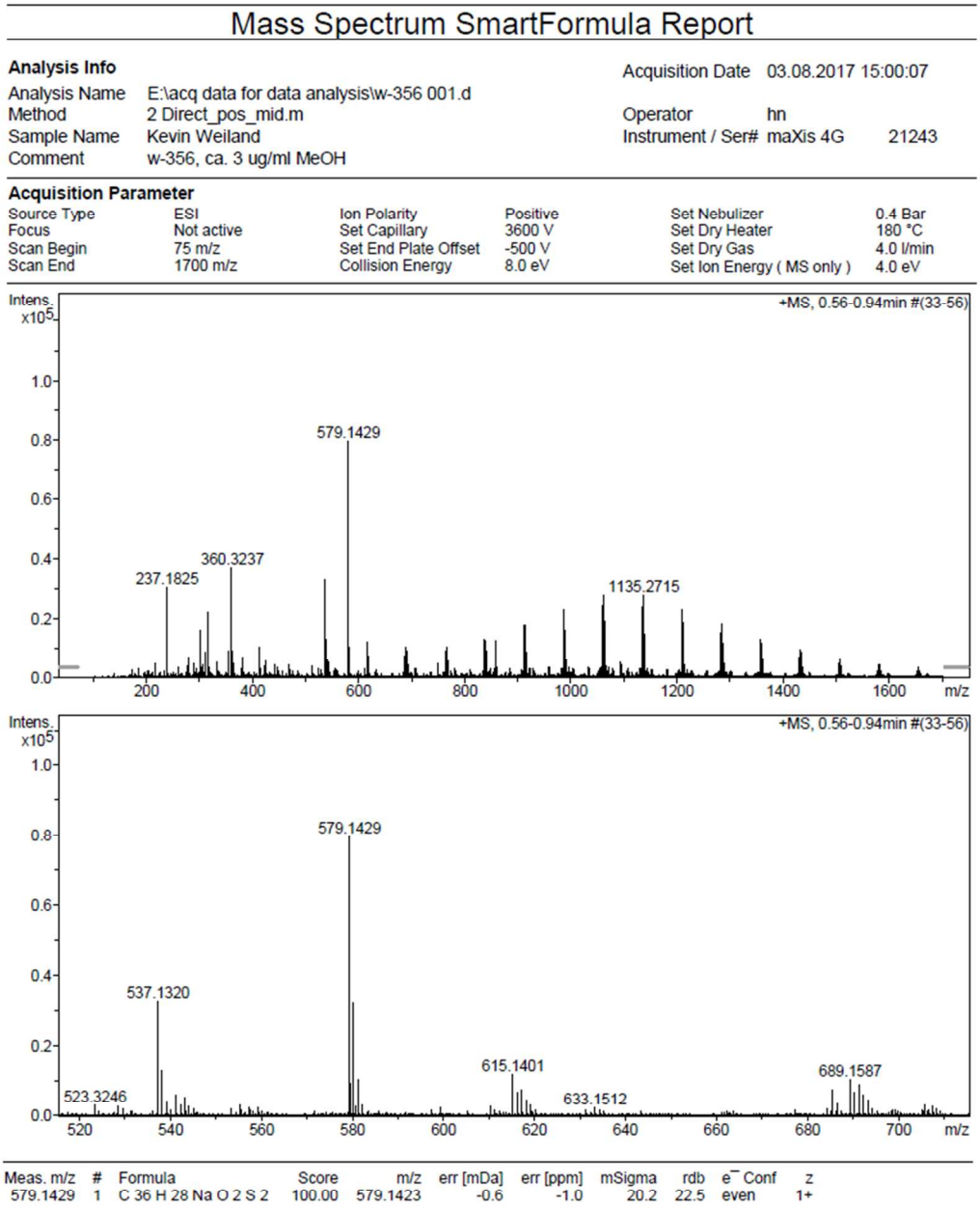

Figure S3. HR ESI spectrum.

3. Crystal data and structure refinement

Table S1 Single crystal data

Empirical Formula	$C_{36}H_{28}O_2S_2$
Formula Weight	556.75
Crystal habit	colorless plates
Temperature/K	123
Crystal system	monoclinic
Space group	P $2_1/n$
a/Å	6.96730(10)
b/Å	10.7521(2)
c/Å	18.3959(3)
α/°	90
β/°	90.5290(10)
γ/°	90
Volume/Å^3	1378.04(4)
Z	2
ρ_{calc}/g cm^{-3}	1.342
μ/mm^{-1}	1.313
F(000)	583.997
Crystal size/mm^3	0.030 x 0.130 x 0.250
Radiation	GaK_α (λ = 1.34143 Å)
Θ_{max}/°	59.338
Reflections collected	27529
Independent reflections	3022 merging (r = 0.028)
Observed reflections	2956
Parameters	181
Goodness-of-fit on F^2	1.0848
Final R indices [I≥2σ(I)]	0.0343
Final R indices [all data]	0.0372
Largest diff. peak hole/e Å^{-3}	-0.31/0.28
CCDC number	1836317

Single crystals suitable for crystal structure determination were grown by slow evaporation of a solution of hexane and dichloromethane at room temperature. The crystal was measured on a Stoe StadiVari. Minimal/maximal transmission 0.84/0.96. The STOE X-AREA suite has been used for data collection and integration. The structure was solved by other methods using the program Superflip. Least-squares refinement against F was carried out on all non-hydrogen atoms

using the program CRYSTALS. Chebychev polynomial weights were used to complete the refinement. Plots were produced using CAMERON. Crystallographic data (excluding structure factors) for the structure in this paper have been deposited with the Cambridge Crystallographic Data Center. Copies of the data can be obtained, free of charge, on application to the CCDC, 12 Union Road, Cambridge CB2 1EZ, UK [fax: +44-1223-336033 or e-mail: deposit@ccdc.cam.ac.uk]. Molecular drawings were generated using Mercury.

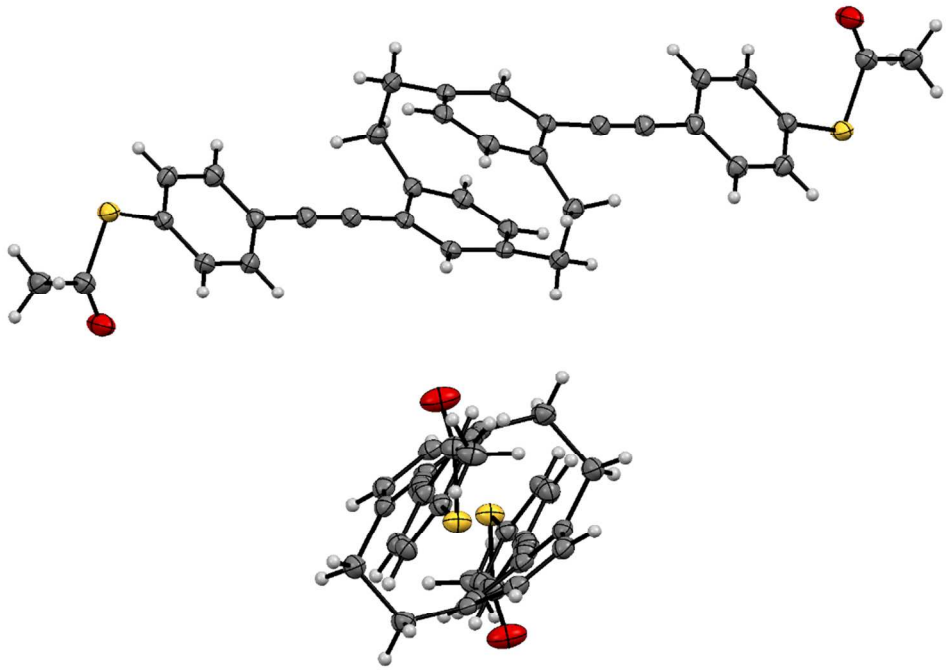

Figure S4. ORTEP diagrams of molecule **1**, ellipsoids shown at the 50% probability level.

Supporting Section II. Transport Measurements

1. Fast-breaking measurements

The conductance histograms for fast-breaking and distance-modulation measurements are displayed in Fig. S5. The most probable conductance values ($3.7 \cdot 10^{-6}$ G_0 and $2.7 \cdot 10^{-6}$ G_0, respectively) match well despite the measurement being performed on different samples and with different techniques. Distance-modulation measurements were recorded for a maximum time of 120 s, and therefore the histogram highlights the most stable configurations, as opposed to the fast-breaking measurements, where metastable ones have a bigger impact on the conductance histogram.

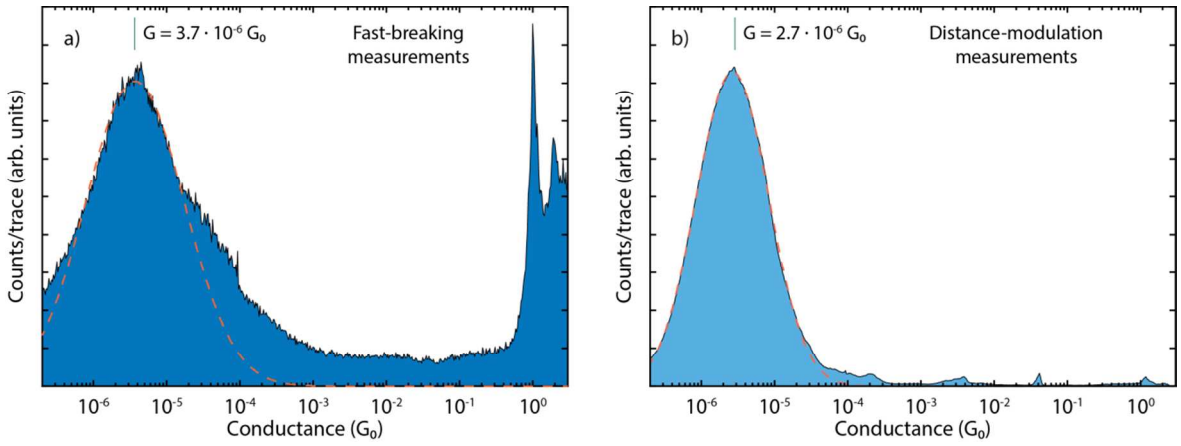

Figure S5. One-dimensional histogram a) of a fast-breaking measurement of sample **A** and b) of a distance-modulation measurement of sample **B**. The applied bias is 100 mV in both cases, fast-breaking measurements were recorded at 4.0 nm/s. The dashed orange line shows the fit result.

Figures S6-S9 show the two-dimensional histograms of samples **A**-**D**. The concentrations of the molecular solution dropcasted were 9 µM for sample **A** and **B**, 90 µM for sample **C**, and 900 µM for sample **D.** As can be seen from the histograms, no significant dependence on the concentration is observed and all samples show similar conductance oscillations.

For each measurement we perform a thorough characterisation of the bare device before dropcasting the molecular solution to ensure that the electrodes are clean and well aligned. The characterisation of the bare device used for sample **A** is shown in Fig. S10.

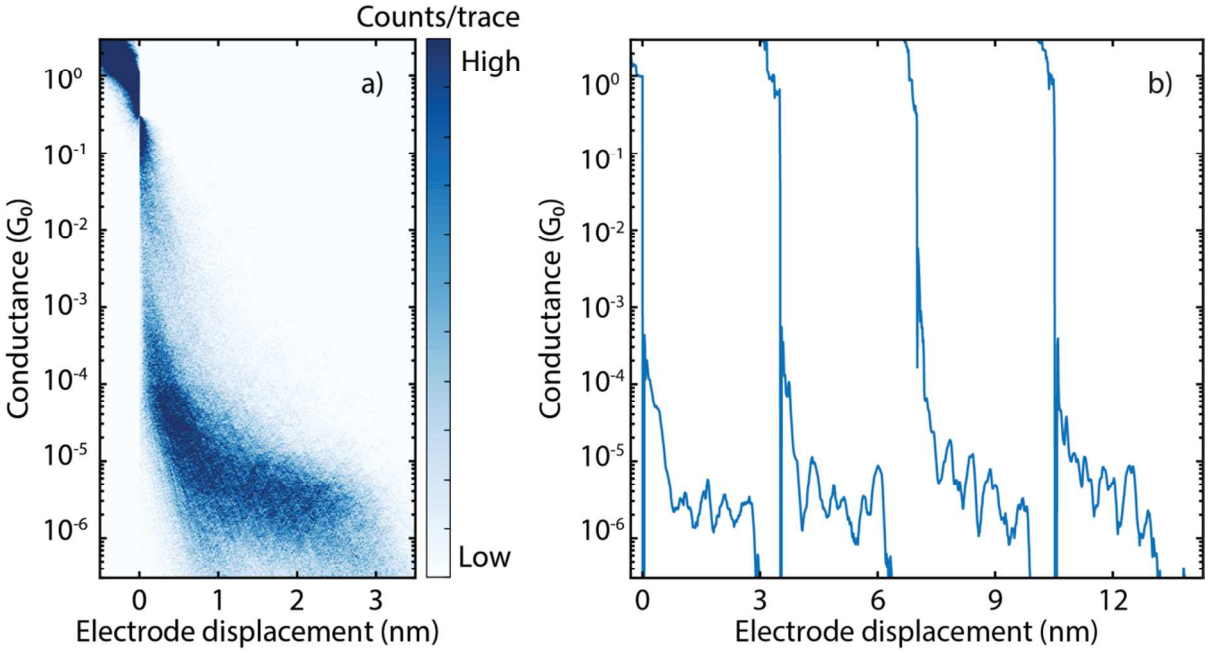

Figure S6. a) Two-dimensional conductance histogram of sample **A** with no data selection. b) Examples of the 3,000 consecutive breaking traces. The applied bias is 100 mV and the electrode speed is 4.0 nm/s.

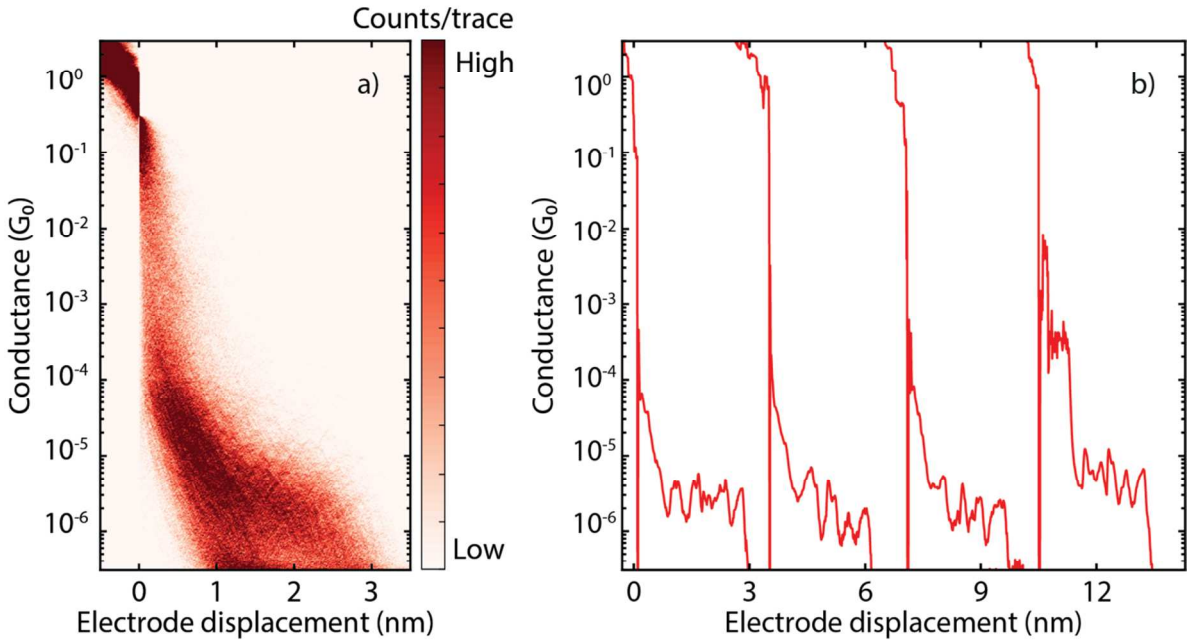

Figure S7. a) Two-dimensional conductance histogram of sample **B** with no data selection. b) Examples of the 3,000 consecutive breaking traces. The applied bias is 100 mV and the electrode speed is 4.0 nm/s.

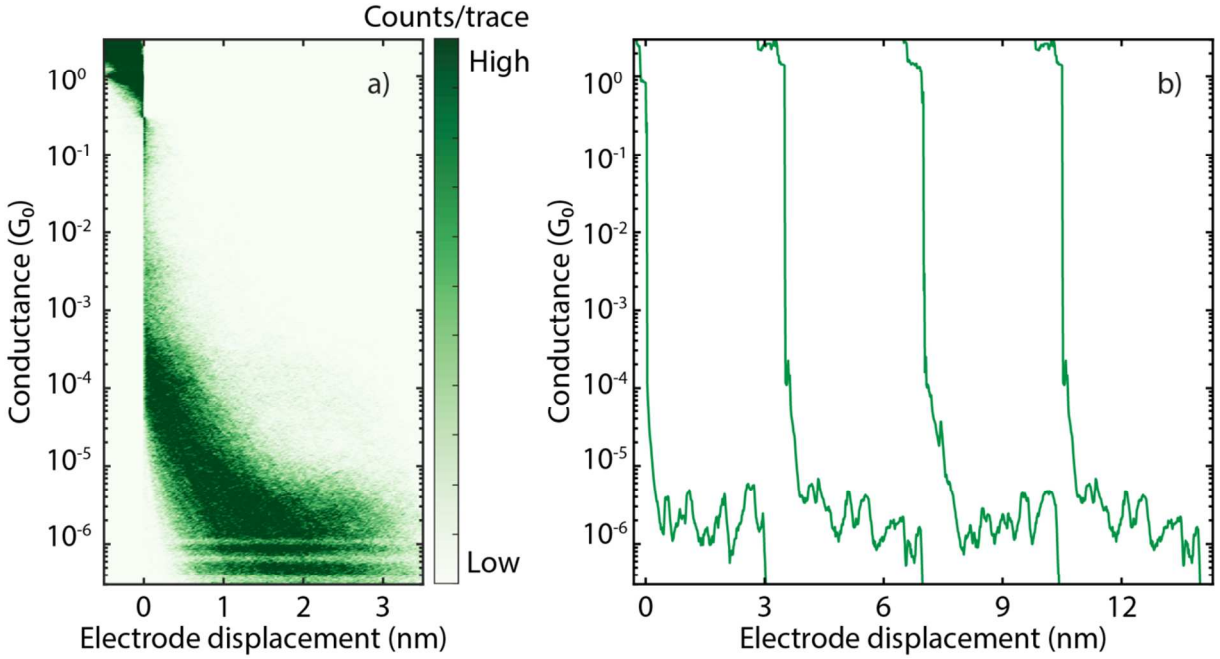

Figure S8. a) Two-dimensional conductance histogram of sample **C** with no data selection. b) Examples of the 3,000 consecutive breaking traces. The applied bias is 100 mV and the electrode speed is 4.0 nm/s.

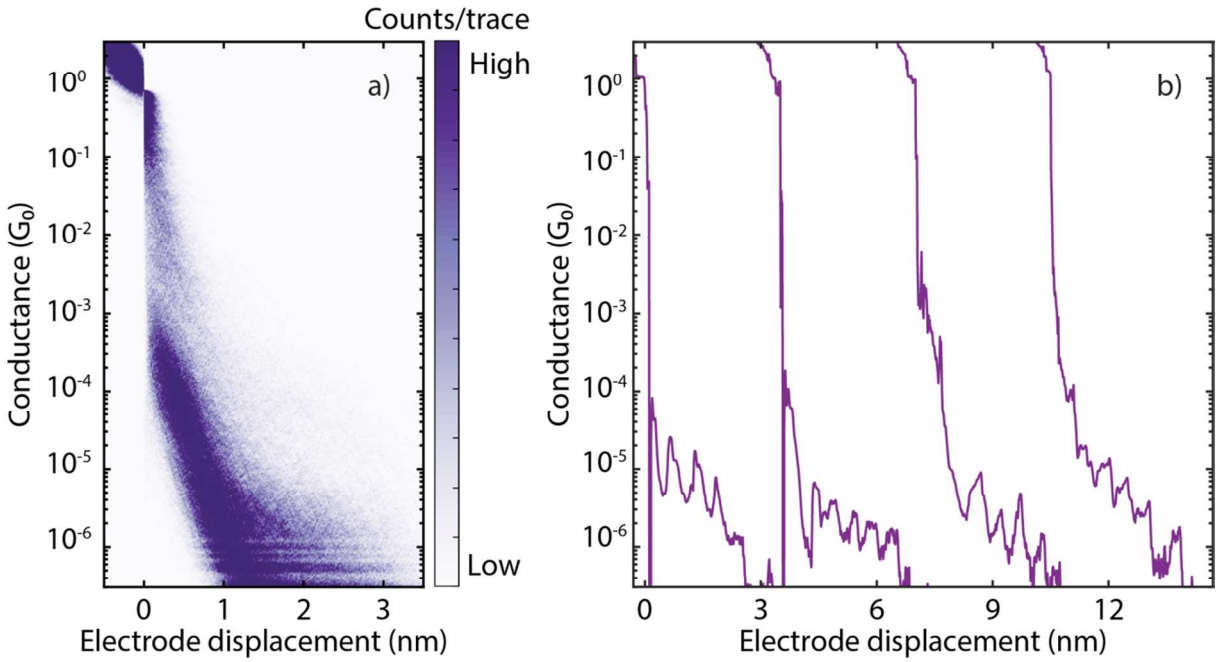

Figure S9. a) Two-dimensional conductance histogram of sample **D** with no data selection. b) Examples of the 5,000 consecutive breaking traces. The applied bias is 100 mV and the electrode speed is 4.0 nm/s.

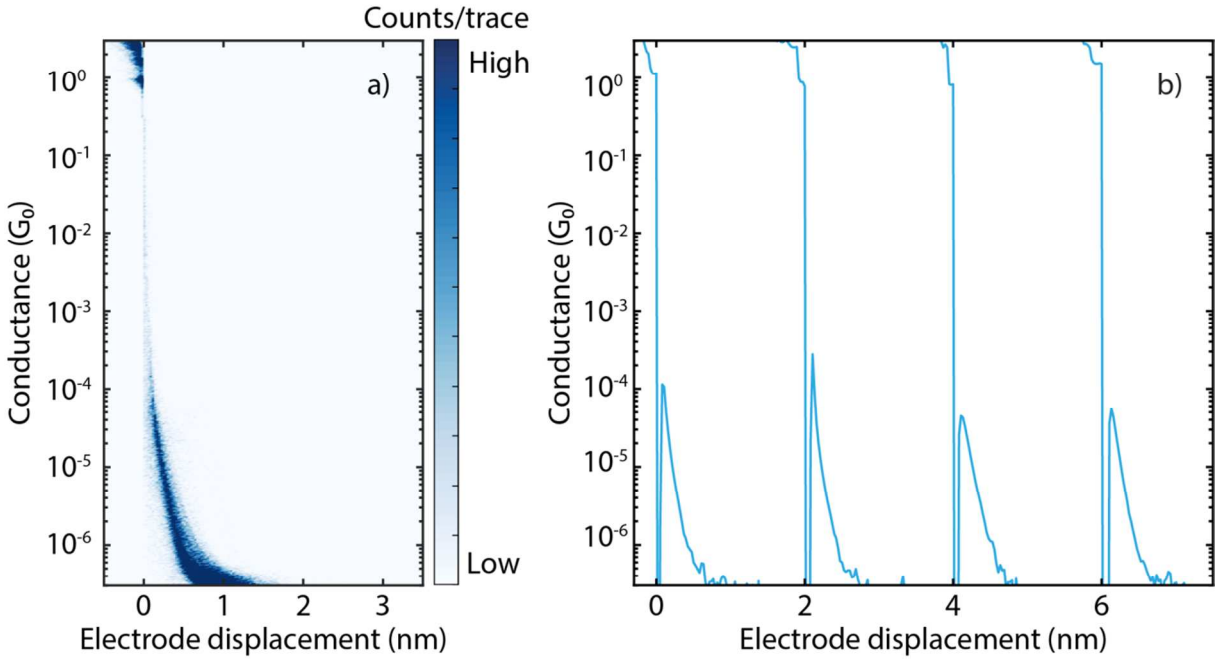

Figure S10. a) Two-dimensional conductance histogram and b) examples of conductance traces from the characterisation of the pristine sample used for measurements **A**. The applied bias is 100 mV and the electrode speed is 8.0 nm/s.

Estimation of the oscillation periodicity

To estimate the periodicity of the conductance variations, we selected 315 breaking traces from the 3,000 of sample **A** that showed particularly clear oscillations. For each trace we then identified the position of peaks with a prominence of at least 30% and calculated the distance between consecutive peaks. We fit a Gaussian to the histogram and find the parameters shown in the inset of Fig. S11.

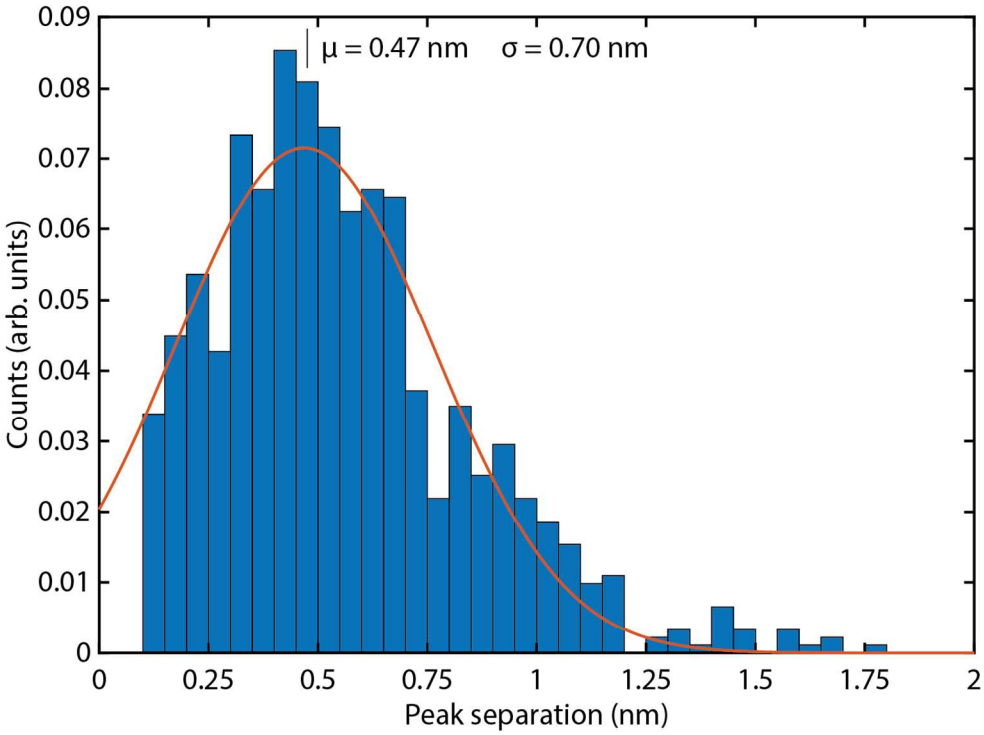

Figure S11. Distribution of the separation between consecutive peaks found in the selected breaking traces from sample **A**. The Gaussian fitted to it is represented as an orange line.

2. Distance-modulation measurements

Additional measurements of sample **B** are shown in Fig. S12. These measurements were taken with a peak-to-peak amplitude of 2.5 Å, smaller than those presented in the main text and in the following figures. Also in this case, both traces in-phase and in antiphase are observed.

More examples of traces in-phase (Fig. S13), in antiphase (Fig. S14) and with doubled frequency (Fig. S15-S16) are reported here. Figure S17 shows a trace for which the behaviour changes from antiphase to in-phase. The inset shows the moment of the transition. Figure S18 presents the Fourier Transform of the distance-modulation traces showing that it is mainly at the same frequency of the driving modulation. Figure S19 shows another full distance-modulation trace with the initial opening of the gap, the gap size modulation, and the final breaking to the noise level.

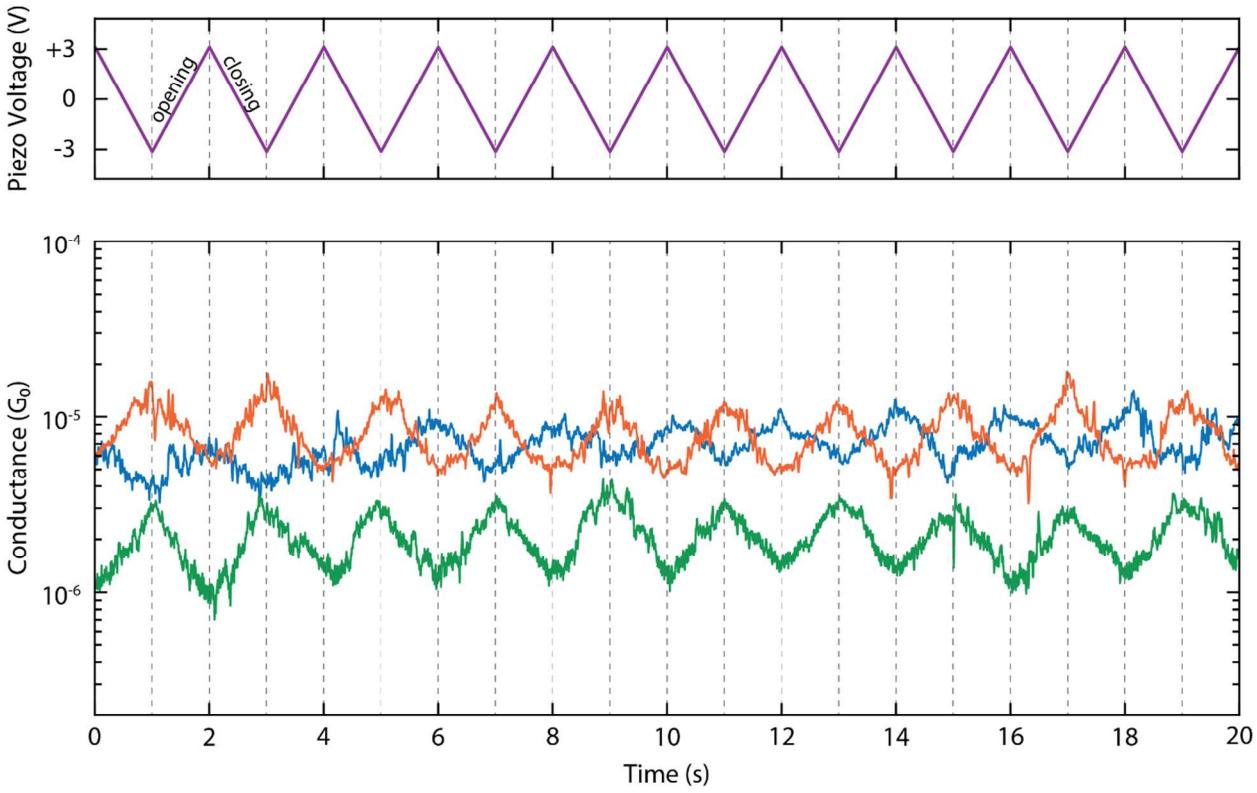

Figure S12. Examples of distance-modulation traces. The total modulation time is 120 s at a frequency of 0.5 Hz. The blue, green and orange lines (bottom panel) represent three different conductance measurements, whereas the purple line (top panel) represents the voltage applied to the piezoelectric stack. The applied piezo voltage translates into a **peak-to-peak distance of 2.5 Å** and a higher voltage corresponds to a larger electrode distance. The conductance responds to the electrode-separation modulation either in-phase (blue curve) or in antiphase (orange and green curves).

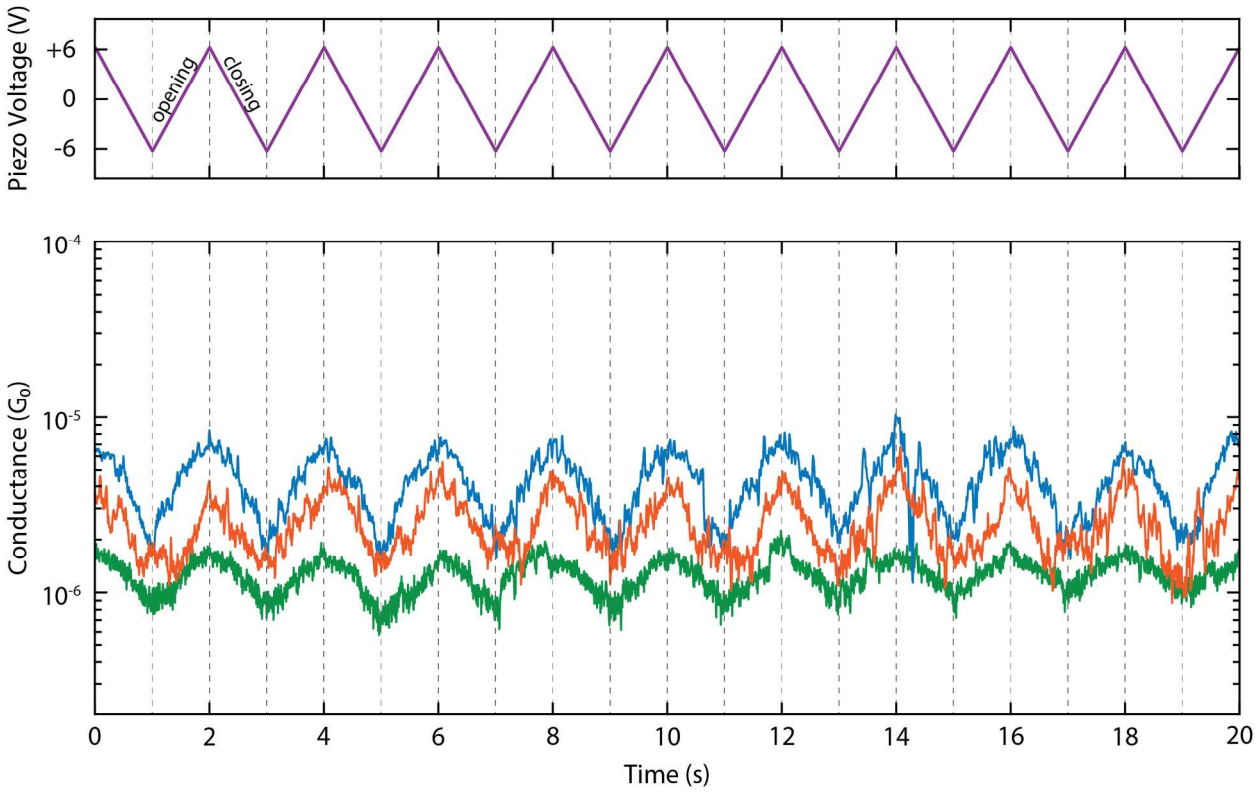

Figure S13. Examples of distance-modulation traces. The total modulation time is 120 s at a frequency of 0.5 Hz. The blue, green and orange lines (bottom panel) represent three different conductance measurements, whereas the purple line (top panel) represents the voltage applied to the piezoelectric stack. The applied piezo voltage translates into a peak-to-peak distance of 5.0 Å and a higher voltage corresponds to a larger electrode distance. In these cases, the conductance responds **in-phase** with the gap-size variation.

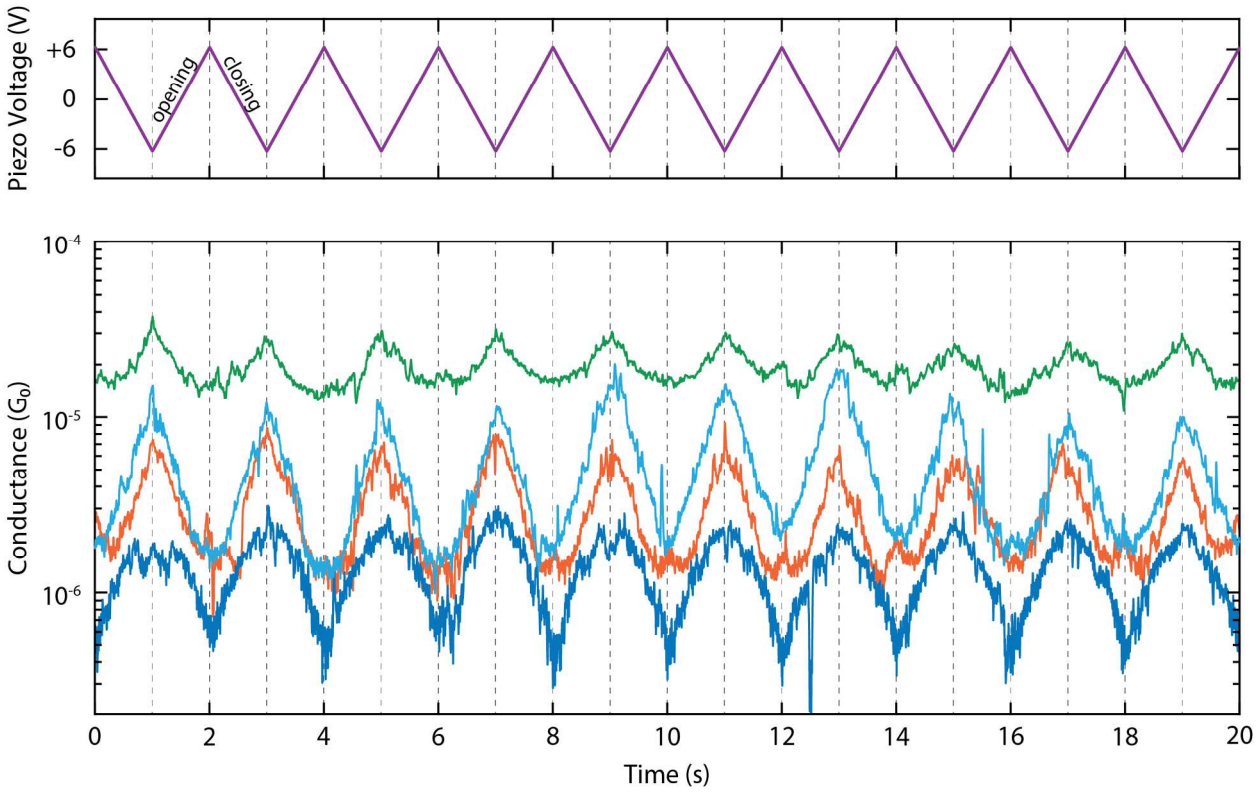

Figure S14. Examples of distance-modulation traces. The total modulation time is 120 s at a frequency of 0.5 Hz. The blue, green, cyan and orange lines (bottom panel) represent three different conductance measurements, whereas the purple line (top panel) represents the voltage applied to the piezoelectric stack. The applied piezo voltage translates into a peak-to-peak distance of 5.0 Å and a higher voltage corresponds to a larger electrode distance. In these cases the conductance responds **in antiphase** with the gap-size variation.

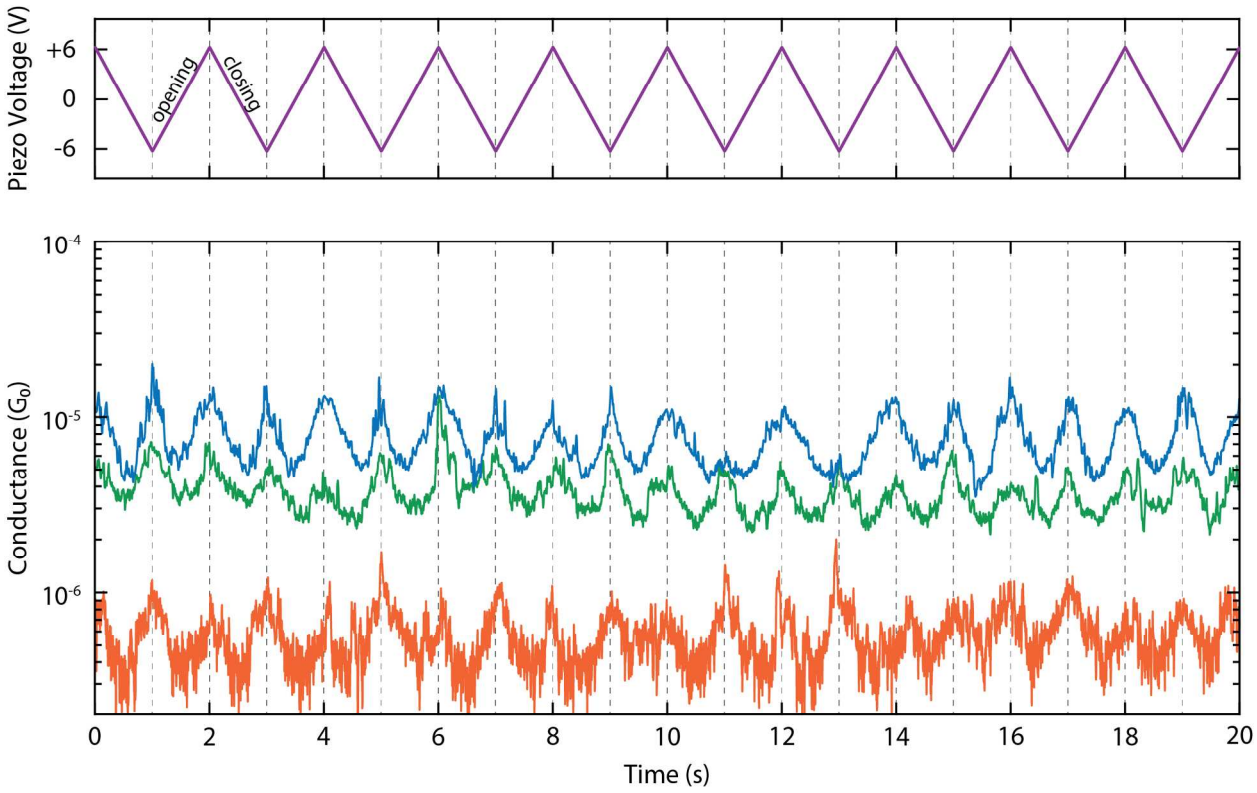

Figure S15. Examples of distance-modulation traces. The total modulation time is 120 s at a frequency of 0.5 Hz. The blue, green and orange lines (bottom panel) represent three different conductance measurements, whereas the purple line (top panel) represents the voltage applied to the piezoelectric stack. The applied piezo voltage translates into a peak-to-peak distance of 5.0 Å and a higher voltage corresponds to a larger electrode distance. In these cases the conductance responds with **double the frequency** of the driving modulation.

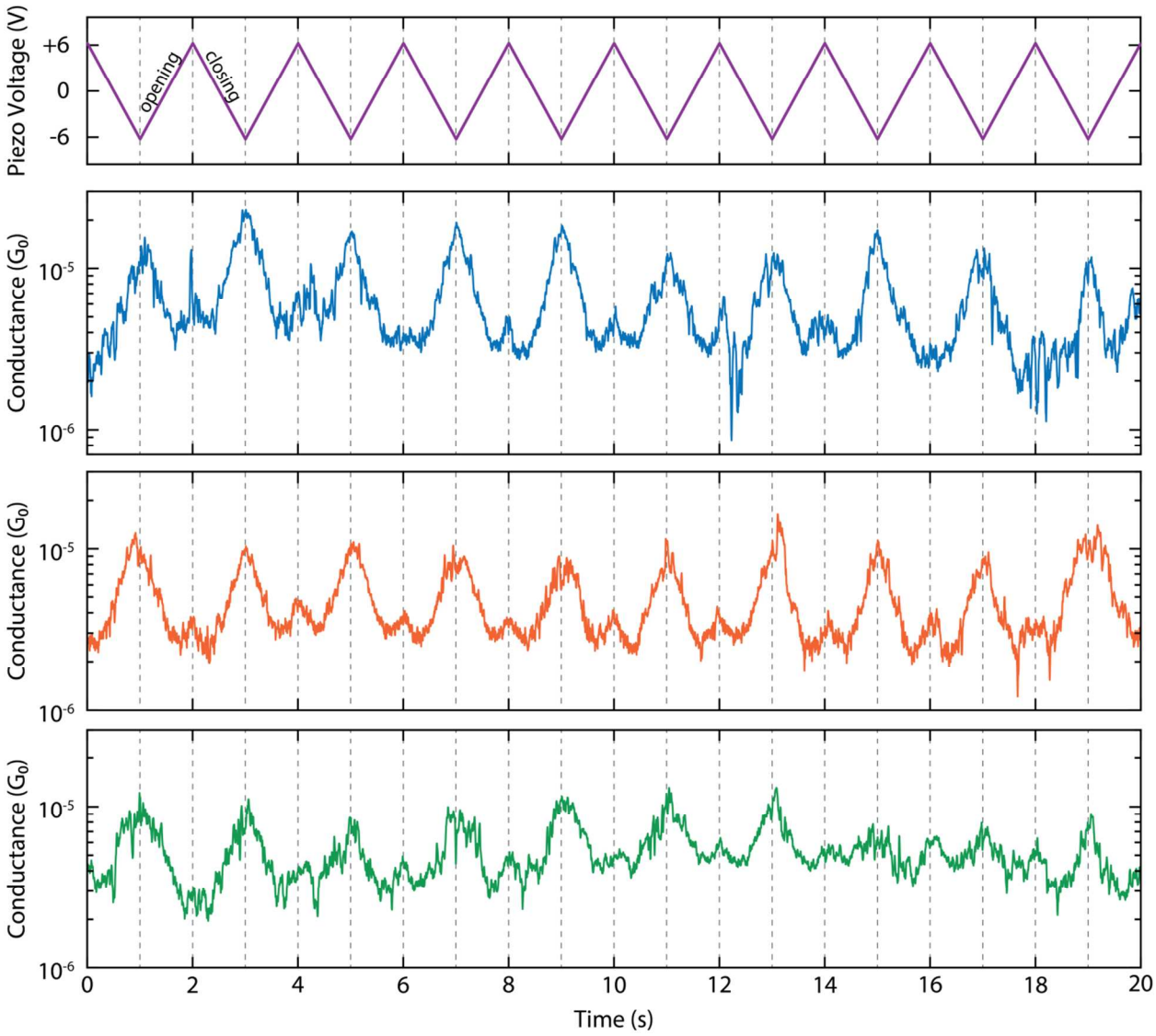

Figure S16. Examples of distance-modulation traces. The total modulation time is 120 s at a frequency of 0.5 Hz. The blue, green and orange lines (bottom panels) represent three different conductance measurements, whereas the purple line (top panel) represents the voltage applied to the piezoelectric stack. The applied piezo voltage translates into a peak-to-peak distance of 5.0 Å and a higher voltage corresponds to a larger electrode distance. In these cases the conductance responds with **double the frequency** of the driving modulation, with subsequent peaks having different heights.

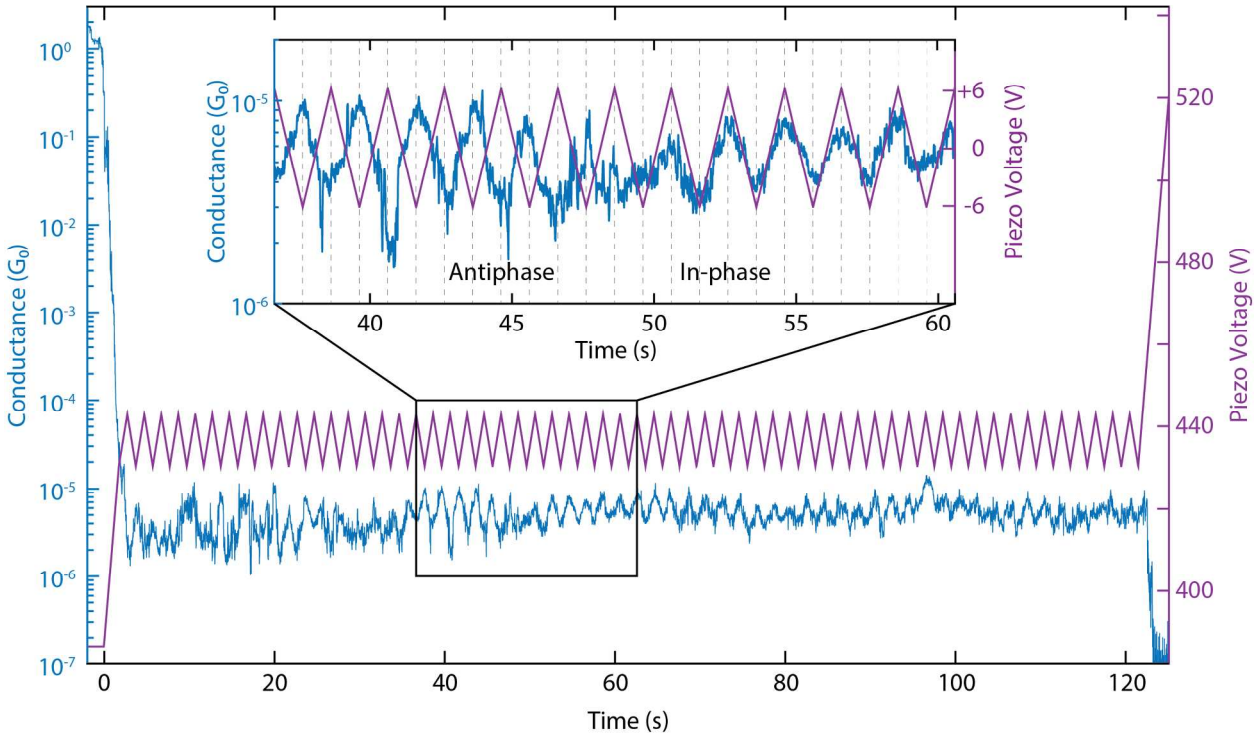

Figure S17. Example of a distance-modulation trace. The total modulation time is 120 s at a frequency of 0.5 Hz. The blue line represents the conductance measurement, whereas the purple line the voltage applied to the piezoelectric stack. The applied piezo voltage translates into a peak-to-peak distance of 5.0 Å, and a higher voltage corresponds to a larger electrode distance. The inset shows a portion of the trace in which a shift from antiphase to in-phase occurs.

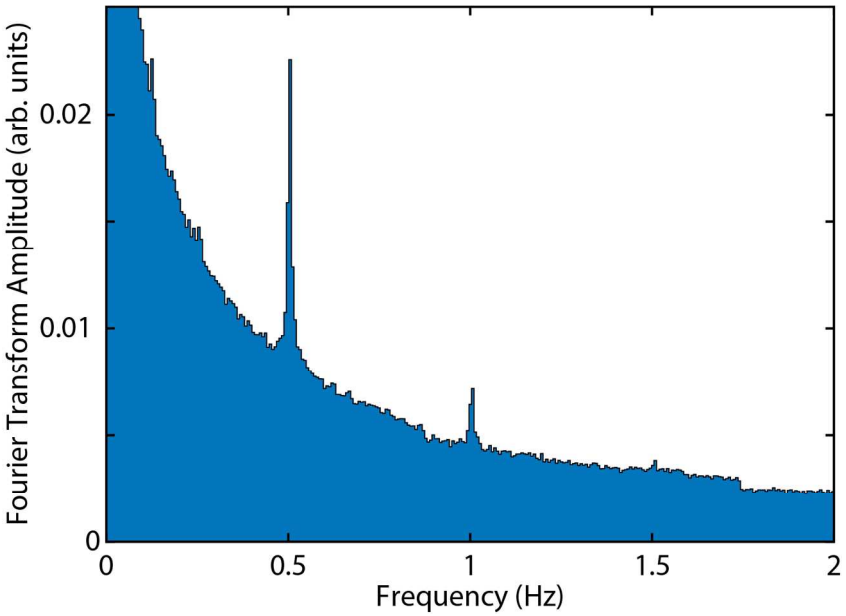

Figure S18. Fourier Transform of the conductance traces measured with a displacement modulation at 0.5 Hz. A pronounced peak is found at the driving frequency of the piezoelectric stack and a smaller one at the second harmonic.

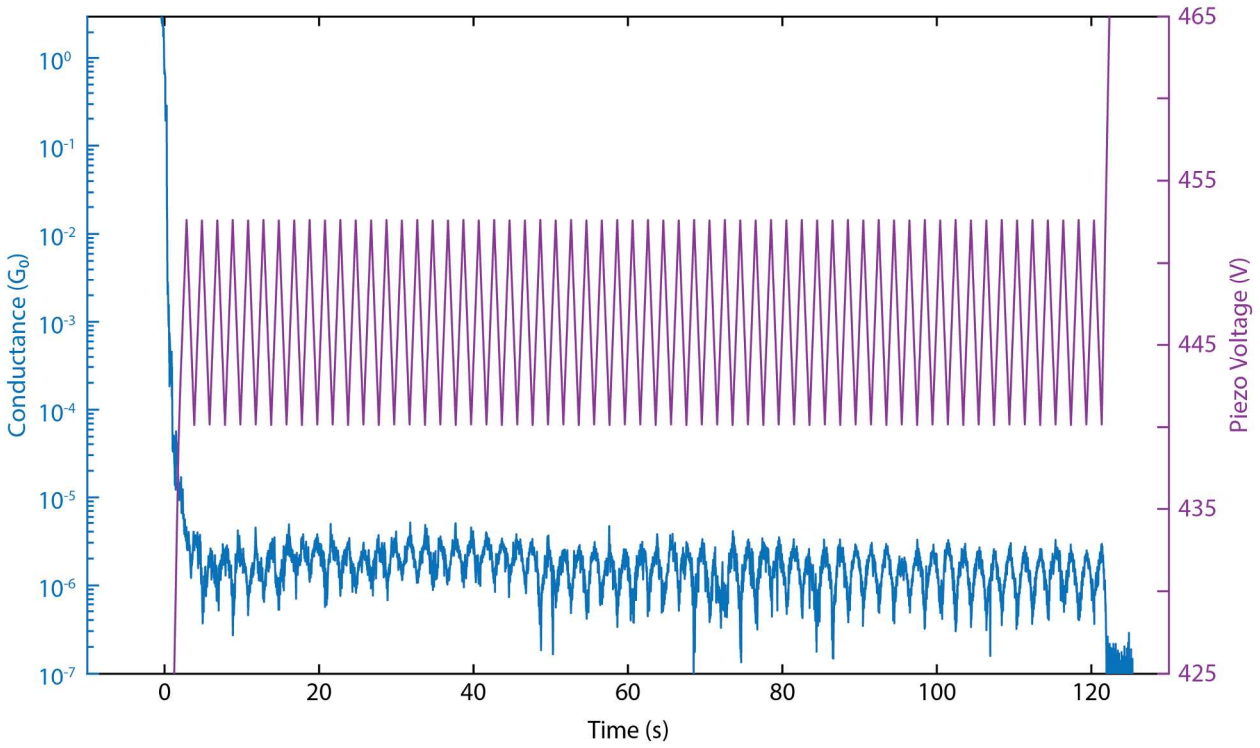

Figure S19. Example of a distance-modulation trace. The full trace is shown here with the initial opening of the gap, the gap size modulation at 0.5 Hz for 120 s, and the final breaking to the noise level. The blue line represents the conductance measurement, whereas the purple line represents the voltage applied to the piezoelectric stack. The applied piezo voltage translates into a peak-to-peak distance of 5.0 Å and a higher voltage corresponds to a larger electrode distance.

3. Statistical analysis

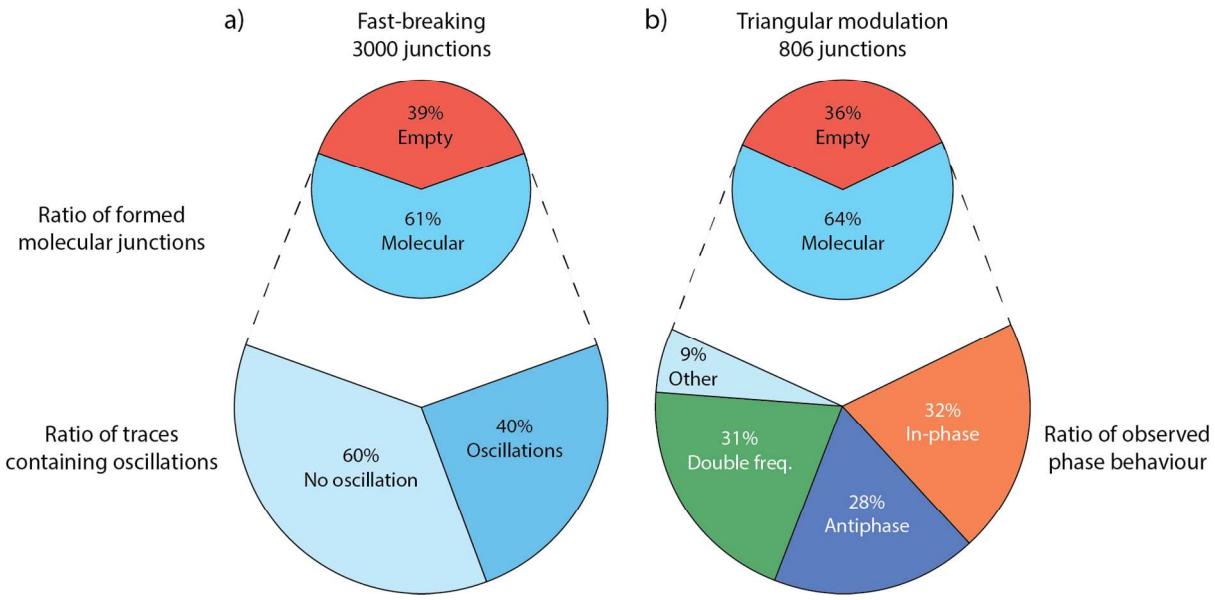

Figure S20. a) Junction-formation statistics and percentage of molecular junctions showing conductance oscillations for fast-breaking measurements (sample **A**). b) Junction-formation statistics and percentage of phase response behaviours of the conductance oscillations in triangular modulation measurements (sample **B**). The percentage of molecular traces is remarkably similar despite the measurements being performed on different samples and with different techniques.

4. Estimation of the gauge factor

The gauge factor of a strain gauge *GF* is defined as the ratio between the change in relative electrical conductance $\Delta G/G$ and the mechanical strain ε. From the distance modulation experiment it is possible to estimate the gauge factor of the molecule. To do so, we selected 123 traces from the 806 of sample **B** that showed particularly clear and stable oscillations. We then split each trace into semi-periods of the piezo modulation, i.e., portions in which the electrodes move in the same direction. For each of these portions we then identified the maxima and minima

in conductance and their respective positions. From the former two, $\Delta G/G$ is extracted by dividing the change in conductance with the average conductance for the portion of trace considered; from the latter, ε is obtained by dividing the electrode displacement (ΔL) by the size of the relaxed molecule (L = 1.75 nm). The *GF* is thus given by:

$$GF = \frac{\frac{\Delta G}{G}}{\varepsilon} = \frac{\frac{\Delta G}{G}}{\frac{\Delta L}{L}}$$

Since the frequency of the modulation was 0.5 Hz for a maximum time of 120 s, each trace can provide up to 120 gauge factor values.

The *GF* distribution is shown in Fig. S21. Both in-phase and antiphase traces were among the selected traces, which means that both positive and negative values in the gauge factor can be obtained: negative gauge factor values are obtained from antiphase traces. The peaks in the distribution are found at *GF* = +5 and *GF* = -7. The distribution of the absolute values is plotted in the main text (Fig. 3b).

This simple method for estimating the *GF* yielded the same qualitative result as others with more restrictive constraints in the peak selection or with preliminary smoothing of the curves, showing that noise spikes do not play an important role in the average result.

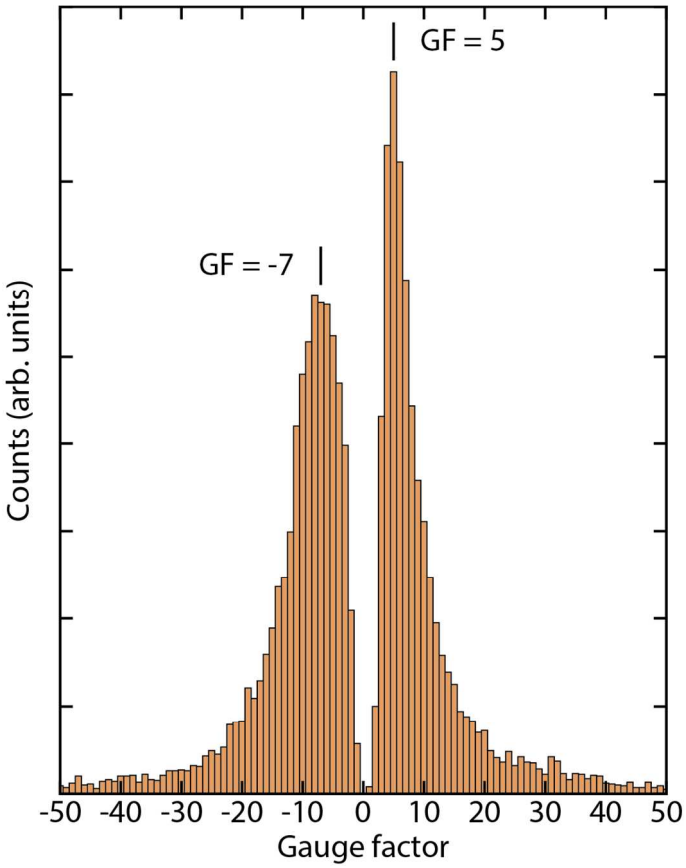

Figure S21. Distribution of gauge factor values obtained from 123 selected traces of the distance-modulation measurements performed on sample **B**.

Supporting Section III. Transport Calculations

1. Setup of DFT simulations

Throughout all DFT calculations we used the def-SVP basis set and the PBE functional.[3,4] During structural relaxations the total energy was converged to 10^{-6} a.u. and the maximum norm of the Cartesian gradient to 10^{-3} a.u. Initial configurations of molecular junctions were obtained in the following way: The gas-phase molecule was relaxed with one gold atom at each sulfur atom. Independently, we relaxed the corresponding gold leads with a benzene ring attached through a sulfur atom. We then combined the relaxed structures to the final system, which we call extended

central cluster (ECC), as described in Bürkle *et al.*[5] In short, this was done by replacing the benzene rings, attached to the leads, with the relaxed molecule. Finally, the obtained system was relaxed once again, giving the initial structure for further molecular junction simulations, in which the lead separation was varied in steps of 0.1 or 0.2 Å.

2. Quantum interference effects

The source of the transmission valley in Fig. 5 lies in the quantum mechanical interference of frontier orbital contributions to the transmission. Its presence can be explained solely by the gas-phase HOMO (GPH) and gas-phase LUMO (GPL). However, the shift in energy of the conductance dip as a function of the displacement can only be explained, if one also takes the GPH-1 and GPL+1 into account. The underlying theory is described in the literature.[6,7] In a toy model, the electronic transmission of our ECC can be expressed as

$$\tau(E) = \frac{\left(2\pi\beta^2\right)^2}{2} G^a(E) G^r(E) \rho_l(E) \rho_r(E) \tag{1}$$

where β is the transfer integral of the gold-sulfur bond, $G^{a/r}(E)$ are matrix elements of the energy-dependent advanced and retarded Green's functions of the molecule that connect terminal sulfur atoms, and $\rho_{l/r}(E)$ are the local densities of states of the left and right leads. The zeroth-order Green's functions, describing a molecular junction, in which the molecule does not interact with the leads, are given as

$$G^{(0)r/a}(E) = \sum_k \frac{C_{l,k} C^*_{r,k}}{E - \epsilon_k \pm i\eta} \tag{2}$$

with the expansion coefficients $C_{l/r,k}$ of the *k*-th molecular orbital at the left/right sulfur atom and the orbital energies ϵ_k. Using $G^{a/r}(E) \approx G^{(0)a/r}(E)$, the transmission can be written as

$$\tau(E) \propto \left| G^{(0)r}(E) \right|^2. \tag{3}$$

A general rule for the conductance, i.e. the transmission at the Fermi energy E_F, can be deduced from Eq. 2: Since $E_F - \epsilon_{HOMO}$ and $E_F - \epsilon_{LUMO}$ have opposite signs, the corresponding summands in the zeroth-order Green's function $G^{(0)r}(E)$,

$$\frac{C_{l,HOMO}C^*_{r,HOMO}}{E_F-\epsilon_{HOMO}+i\eta} + \frac{C_{l,LUMO}C^*_{r,LUMO}}{E_F-\epsilon_{LUMO}+i\eta}, \tag{4}$$

will have the same (different) signs, if the products $C_{l,HOMO}C^*_{r,HOMO}$ and $C_{l,LUMO}C^*_{r,LUMO}$ have different (same) signs. The sign of each coefficient $C_{l/r,k}$ corresponds to the sign of the wave function *k* at the particular site *l,r*, i.e. on the electrode-connecting sulfur atoms.

The HOMO and LUMO in the molecular subspace of our ECC at displacements close to the observed transmission valley (precisely, for displacements *d* with -1 Å < *d* < 2 Å) are related to the GPH and GPL, respectively (Fig. 5c). Since these molecular orbitals are centrally symmetric, the coefficients $C_{l/r,k}$ need to be of the same sign for each orbital at the left and right sites. As a consequence the products $C_{l,k}C^*_{r,k}$ yield identical signs for both orbitals, which finally leads to an antiresonance in the transmission $\tau(E)$ at an energy $\epsilon_{HOMO} < E < \epsilon_{LUMO}$.

The shift of this energy upon mechanical deformation can be explained, if we take also the HOMO-1 and LUMO+1 (attributed to GPH-1 and GPL+1) into account. To illustrate this, we calculate the conductance according to Eq. 3 for a toy model system, which has four molecular orbitals with displacement-dependent energies $\epsilon_k(d) \coloneqq a_k \arctan(b_k + \mathrm{d}) + \epsilon_k^0$, where $k \in \{\mathrm{HOMO}-1, \mathrm{HOMO}, \mathrm{LUMO}, \mathrm{LUMO}+1\}$. The coefficients a_k, b_k and ϵ_k^0 are chosen to mimic the energy dependence of the orbitals according to the DFT results in Fig. 5c. The products $C_{l,k}C^*_{r,k} =: c_k$ were chosen according to the symmetries of the gas-phase molecular orbitals of the studied molecule from Fig. 4a: $c_k = \pm 1$ for centrally symmetric/antisymmetric wave functions. Figure S22 shows the resulting transmission map on the left side. The map on the right side

shows the transmission of an extended toy model, where we additionally assume four more molecular orbitals (eight in total) at displacement-independent energies of -1.4, -1.2, 5 and 8 eV with products c_k equal to -1, 1, 1 and -1.

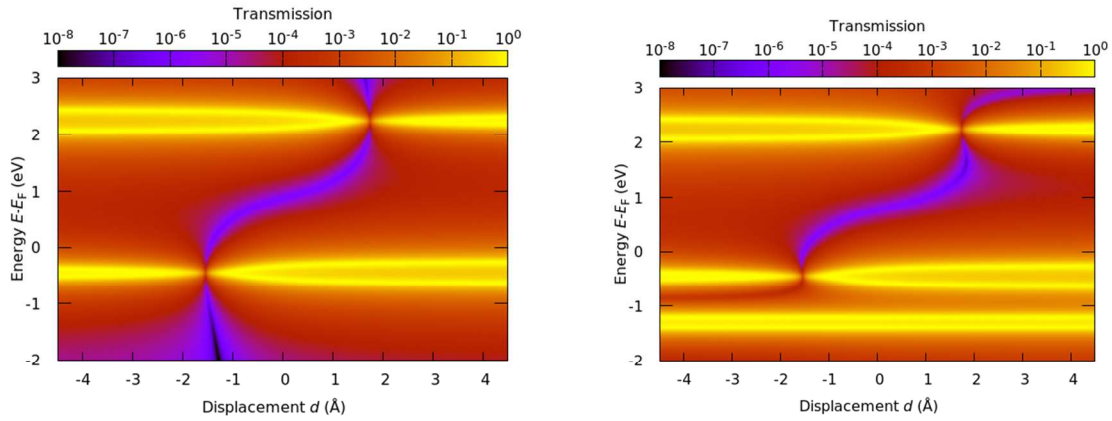

Figure S22. Calculated transmission of a toy model. The molecular orbital energies and their dependence on the displacement (causing the horizontal yellow traces) were modelled in such a way as to mimic the traces obtained from the DFT calculations in Fig. 5. The simpler model (left map) considers four orbitals, while the refined model (right map) additionally considers four more displacement-independent orbitals (of which only two are visible in the chosen energy range).

An antiresonance with a clear displacement dependence occurs between the frontier orbitals within this toy model. The antiresonance crosses the orbital energies, where GPH-1, GPH and GPL, GPL+1 degenerate. This exactly matches the observations made in the DFT transmission map, although the shape of the antiresonance valley is slightly different. The position of the antiresonance depends on the relative energy distances $\Delta_H \coloneqq \epsilon_{GPH} - \epsilon_{GPH-1}$ and $\Delta_L \coloneqq \epsilon_{GPL+1} - \epsilon_{GPL}$. At $d = -1.5$ Å GPH-1 and GPH degenerate and $\Delta_H = 0$. Since GPH and GPH-1 energies are equal and their coefficients are of opposite sign ($c_{GPH-1} = -1$ and $c_{GPH} = +1$) the corresponding summands in Eq. 2 cancel out. Therefore, at $d = -1.5$ Å the orbitals GPH-1 and

GPH do not contribute to the total conductance. For $d < -1.5$ Å GPH-1 and GPH change their order so that $\Delta_H < 0$. Now the HOMO-1 is attributed to the GPH and the HOMO to the GPH-1. This means that HOMO and LUMO are of different symmetries, which, according to the argument above, leads to summands of the same sign and the resulting contributions to the conductance add up in a constructive manner. In this case there is no antiresonance between the HOMO and the LUMO anymore. An analogous explanation for the vanishing of the destructive interference can be given for $d > 1.8$ Å, where GPL and GPL+1 change their energetic order ($\Delta_L < 0$).

3. Displacement dependence of molecular orbital energies

As stated above, the displacement dependence of the orbital energies is crucial for the theoretical explanation of the displacement-dependent transmission. The isovalue plots of the four frontier orbitals are shown in Fig. 5a. These are sufficient to understand the displacement dependence of the orbital energies. First, we consider the GPH and GPL: Starting from $d = 0$ Å (near the total energy minimum at 0.2 Å, where the molecule is closest to its gas-phase configuration) their energies increase, if the molecule is stretched (see Fig. 5c). The reason for this is the shifting of the stacked benzene rings.

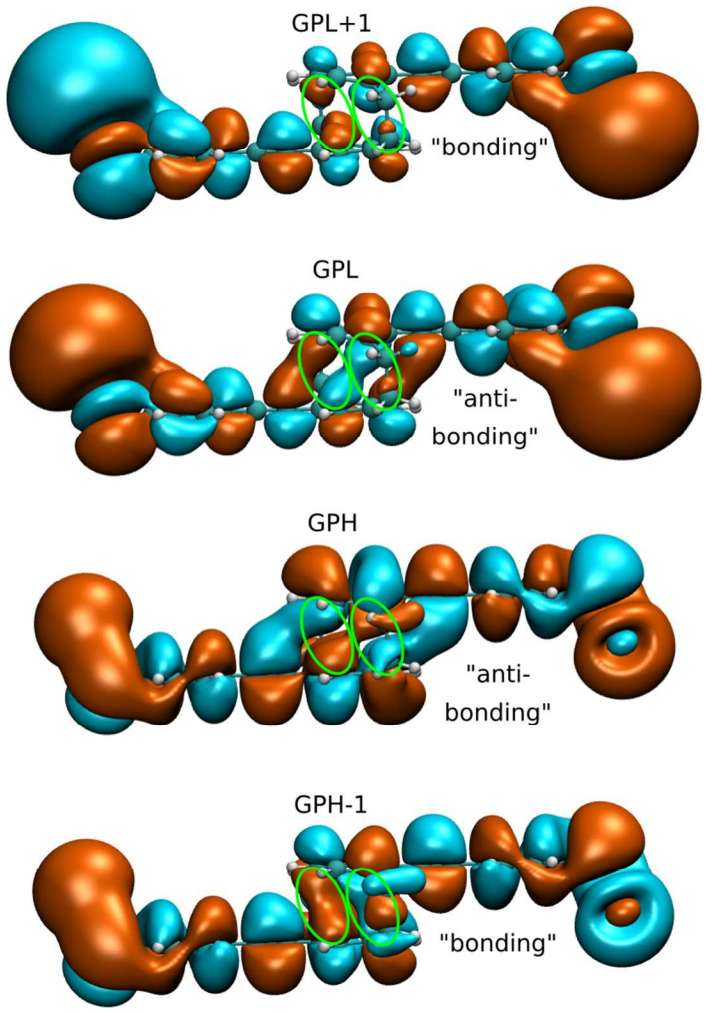

Figure S23. Molecular orbitals of the gas phase configuration. The sulfur atoms are terminated with one gold atom each. Green circles mark the parts of the wave function which arise from the π-orbitals of the stacked benzene rings. These parts show a sign change for GPH and GPL and no sign change for GPH-1 and GPL+1.

The wave function at the opposing stacked rings shows a sign change for GPH and GPL, marked with green circles in Fig. S23, which corresponds to an antibonding configuration. Upon stretching these π-orbitals are brought closer together, thereby increasing the energy. Additionally, the π-orbitals of each OPE unit are moved away from the orbitals arising from the

ethynyl atoms of the other unit, which have the same sign and therefore correspond to a bonding configuration, which as well increases the orbital energy. We can use an analogous argumentation to justify the decrease of the orbital energy of the two other frontier orbitals, GPH-1 and GPL+1. Here, the opposing π-orbitals have the same sign and are in a bonding configuration. If the molecule is stretched, these π-orbitals are brought closer to each other and are removed from the energetically unfavourable ethynyl-chain orbitals, which reduces the orbital energy.

If the benzene rings are shifted too far, the energy change can even be reversed. This is observed, e.g., for the trace caused by GPL+1 in Fig. 5c. Starting from d = 0 Å at first, it moves to lower energies and from d = 3 Å back to higher ones. This happens because the benzene rings are shifted far enough that the π-orbitals start to feel the presence of the next neighbour orbitals of the other OPE unit, which are again of opposite sign. This corresponds to a transition from a bonding to an antibonding configuration, which results in an increase of orbital energy.

4. Choice of displacement scale

The conductance dip in Fig. 5b occurs when the transmission valley intersects the Fermi energy. The displacement at which this intersection takes place is affected by the energies of the frontier orbitals and their couplings to the leads (i.e. by the lead-molecule bonds). In the system presented in Fig. 5 the conductance dip and the minimum of the total energy are separated by 0.2 Å. In other simulated configurations (not presented here) with a different pair of leads, the conductance dip and total energy minimum were separated by a larger distance of around 1 Å.

Since only relative displacements are physically meaningful, we have chosen the zero displacement to coincide with the minimum of the conductance in Fig. 5. Instead, the vanishing displacement in Fig. 4 is determined by the initial geometry.

Due to well-known issues of DFT the calculated molecular orbital energies are likely to be offset compared to the real quasiparticle energies. Beyond absolute conductance values, this implies that there are uncertainties in the DFT with regard to the exact position of the conductance dip as a function of the displacement. However, the qualitative results discussed here, including the occurrence of an antiresonance feature that is sensitive to the stress in the molecule, are well explained.

References

(1) Bondarenko, L.; Dix, I.; Hinrichs, H.; Hopf, H. *Synthesis* **2004**, *2004*, 2751–2759.
(2) Shi, Z.; Wang, L.; Wang, H.; Cao, X.; Zhang, H. *Org. Lett.* **2007**, *9*, 595–598.
(3) Schäfer, A.; Horn, H.; Ahlrichs, R. *J. Chem. Phys.* **1992**, *97*, 2571–2577.
(4) Perdew, J.; Burke, K.; Ernzerhof, M. *Phys. Rev. Lett.* **1996**, *77*, 3865–3868.
(5) Bürkle, M.; Viljas, J.; Vonlanthen, D.; Mishchenko, A.; Schön, G.; Mayor, M.; Wandlowski, T.; Pauly, F. *Phys. Rev. B* **2012**, *85*.
(6) Yoshizawa, K.; Tada, T.; Staykov, A. *J. Am. Chem. Soc.* **2008**, *130*, 9406–9413.
(7) Nozaki, D.; Lücke, A.; Schmidt, W. *J. Phys. Chem. Lett.* **2017**, *8*, 727–732.